DeepEIT: Deep Image Prior Enabled Electrical Impedance Tomography

Dong Liu, *Senior Member, IEEE*, Junwu Wang, Qianxue Shan, Danny Smyl, Jiansong Deng, and Jiangfeng Du

***Abstract*—Neural networks (NNs) have been widely applied in tomographic imaging through data-driven training and image processing. One of the main challenges in using NNs in real medical imaging is the requirement of massive amounts of training data – which are not always available in clinical practice. In this article, we demonstrate that, on the contrary, one can directly execute image reconstruction using NNs without training data. The key idea is to bring in the recently introduced deep image prior (DIP) and merge it with electrical impedance tomography (EIT) reconstruction. DIP provides a novel approach to the regularization of EIT reconstruction problems by compelling the recovered image to be synthesized from a given NN architecture. Then, by relying on the NN's built-in back-propagation and the finite element solver, the conductivity distribution is optimized. Quantitative results based on simulation and experimental data show that the proposed method is an effective unsupervised approach capable of outperforming state-of-the-art alternatives.**

***Index Terms*—Deep image prior, electrical impedance tomography, image reconstruction, neural network, unsupervised learning.**

I. Introduction

IMAGE reconstruction is one of the most challenging aspects of medical imaging [1], [2], since the problem is often ill-posed. Traditionally, regularization schemes, e.g., Tikhonov, total variation, and smoothness prompting prior approaches, are usually used to address this issue. Recently, however, deep learning methods have shifted the attention in the field towards new imaging formulations [3]. For example, supervised networks learn how to execute image reconstruction based on labeled training data, and then optimize the image (under reconstruction) through training procedures [4]. Being task specific, these networks rely heavily on large amounts of training data. However, the range of problems they are able to handle can be constrained by their reliance on training data, which is often difficult or expensive to obtain, especially in medical applications.

Apart from using training sets to perform supervised learning, unsupervised learning [5] has the ability to learn via the NN itself, thus extracting information resembling/corresponding to the input context. For example, untrained convolutional neural networks (CNNs) have proven to be highly effective tools for tackling inverse problems by simply fitting a NN model to the input context (e.g., measurements from an image domain) without any extra training data [6], [7], [8], [9]. The advantage of untrained CNNs was first noted in the deep image prior (DIP) article [6].

Rather than taking a supervised avenue, as many earlier methods have, DIP permits the deep network itself to implicitly handle the regularization task in inverse problems without training data. More specifically, DIP naturally regularizes the reconstruction problem and optimizes the network's parameters for it to synthesize the measurements. DIP has been demonstrated to be effective on several inverse problems, and has achieved remarkable performance on a number of reconstruction tasks in medical imaging modalities, e.g., positron emission tomography [10], computed tomography [11] and magnetic resonance imaging [12].

Inspired by the preceding works, we apply the DIP framework to the field of electrical impedance tomography (EIT). This is, to the best of our knowledge, the first contribution of DIP to image reconstruction in soft-field tomographies. The proposed method discussed here is, however, not limited to EIT. The proposed framework handles the task of recovering images and may consequentially be used for other applications requiring image reconstruction, e.g., diffuse optical tomography [13] and electrical capacitance tomography [14].

EIT, being a functional imaging modality, may help with the management and monitoring of COVID-19 patients [15]. The spatial resolution of EIT is still limited by the intrinsic

Manuscript received 14 August 2022; revised 14 December 2022; accepted 23 January 2023. Date of publication 1 February 2023; date of current version 30 June 2023. This work was supported in part by the National Natural Science Foundation of China under Grants 61871356, 12171453, and 81788101, in part by the National Key Research and Development Program of China under Grant 2018YFA0306600, and in part by the Chinese Academy of Sciences under Grants XDC07040200 and GJJSTD20170001. Recommended for acceptance by S. K. Zhou. *(Corresponding author: Dong Liu.)*

Dong Liu is with the Division of Life Sciences and Medicine, University of Science and Technology of China, Hefei 230026, China, with the CAS Key Laboratory of Microscale Magnetic Resonance, University of Science and Technology of China, Hefei 230026, China, with the Synergetic Innovation Center of Quantum Information and Quantum Physics, University of Science and Technology of China, Hefei 230026, China, and also with the School of Biomedical Engineering and Suzhou Institute for Advanced Research, University of Science and Technology of China, Hefei 230026, China (e-mail: dong.liu@outlook.com).

Junwu Wang and Jiansong Deng are with the School of Mathematical Sciences, University of Science and Technology of China, Hefei 230026, China (e-mail: wangwuj@mail.ustc.edu.cn; dengjs@ustc.edu.cn).

Qianxue Shan and Jiangfeng Du are with the School of Physical Sciences, University of Science and Technology of China, Hefei 230026, China (e-mail: shanqianxue@gmail.com; djf@ustc.edu.cn).

Danny Smyl is with the Department of Civil, Coastal, and Environmental Engineering, University of South Alabama, Mobile, AL 36688 USA (e-mail: dsmyl@southalabama.edu).

Color versions of one or more figures in this article are available at https://doi.org/10.1109/TPAMI.2023.3240565.

Digital Object Identifier 10.1109/TPAMI.2023.3240565

ill-posed nature. Improving EIT image resolution is critical for a variety of applications, such as lung monitoring [16], [17] and brain imaging [18]. For the past decades, various efforts[1] are devoted to exploiting NNs to improve EIT image quality. For example, the article in [19] proposed a CNN based Deep D-bar method for image post-processing and improving the EIT image quality. Meanwhile, CNN was applied to the D-bar reconstruction algorithm for obtaining boundary-enhanced EIT reconstruction [20]. The authors of [21] also employed a CNN, but they trained and learned the mapping between ground-truth conductivity and the conductivity which is obtained from the dominant part of induced contrast current, thereby allowing image quality improvements. A data-driven approach for predicting the conductivity distribution was proposed in [22], where the CNN was used as the solver for EIT reconstruction. In [23], a variational auto-encoder was used to produce a compact and dense representation for lung EIT images with a low dimensional latent space, and then the relationship between the EIT data and the low dimensional latent data was learned. Conditional generative adversarial networks were used in [24] to learn the mapping between the initial image (obtained with the traditional reconstruction methods) to the ground truth. A multi-layer auto-encoder framework was proposed in [25] to learn the nonlinear mapping between EIT measurements and conductivity distributions. Recently, a multi-scale feature cross fusion network [26] was used to reconstruct the EIT image from EIT data and a binary mask image. These approaches to solving EIT problems currently achieve state-of-the-art reconstruction quality. However, they require large amounts of training data, i.e., pairs of ground truths (conductivity distribution) and measurements, and it is unclear how much data is required for achieving good generalization. Practically, ground truth information is difficult to obtain, since the conductivity distribution inside the human body cannot be measured directly.

In this article, rather than using NNs as a training tool, we propose to bring in the DIP architecture regularization effect into the reconstruction problem and directly conduct image reconstruction using NNs without training data. The key idea is to convert the EIT image reconstruction problem into a NN parameter optimization problem. Then, by relying on the NN's back-propagation and the finite element solver, the conductivity distribution is determined. A side effect of reconstructing the EIT image via optimizing NN's parameters is that the framework is afforded the ability to extract high resolution boundary information at no additional cost. We demonstrate the efficacy of our proposed approach by using numerical simulations and water tank data. In this, we obtain better reconstructions than the state-of-the-art methods in terms of perceptual and quantitative metrics.

The structure of the article is organized as follows. In section II, we briefly describe the EIT forward and inverse problems. Section III presents the DIP framework based EIT reconstruction. Next, we provide the implementation details and results in Sections IV and V, respectively. Section VI discusses the opportunities, challenges and robustness issues of the proposed approach. Lastly, conclusions are presented in Section VII.

[1]Given the objective of this article, the literature review is limited here to recent works on using NNs for EIT.

II. Electrical Impedance Tomography

Generally, the EIT reconstruction algorithm involves solutions to forward and inverse problems. The forward problem is to compute the boundary measurements V from a given conductivity σ within the measurement domain Ω. Since the measurement V is non-linearly dependent on the distribution σ, numerical methods, e.g., the finite element method, are often used for finding solutions to the forward problem. In this work, the non-linearity is numerically manifested via the finite-element version of the complete electrode model [27]. For numerically approximating the CEM using finite element analysis, the reader is referred to [28]. If we write down the noiseless observation model as follows

$$V = U(\sigma), \tag{1}$$

then, the EIT inverse problem is to determine σ from the measurement V through the numerical forward model U. To obtain a solution to the problem described in (1) we minimize the following function

$$\hat{\sigma} = \arg\min_{\sigma} \|V - U(\sigma)\|^2 . \tag{2}$$

Note that a diffusive physical nature makes the EIT problem severely ill-posed. It is therefore common to regularize the reconstruction task by constraining the solution using some prior knowledge. In practice, an explicit regularizer $R(\sigma)$, constraining the solution to the desired conductivity properties, is often added in the minimization problem (2). As a simple but representative example, $R(\sigma)$ can be selected as total variation (TV) regularization, which encourages the solution to be sparsity prompting [29]. However, in this article, we mainly focus on developing the DIP based framework and exploring its implicit regularization effect. As an instructive purpose, we briefly analyze the DIP in combination with classical explicit TV regularization in the discussion section.

III. DeepEIT: Deep Image Prior Based EIT

In this section, we begin by providing a brief introduction to DIP framework. Following, we discuss how to utilize DIP in combination with EIT reconstruction, i.e., applying DIP for conducting EIT image reconstruction without training data.

A. DIP Framework

Recently, Ulyanov et al. [6] proposed a DIP framework, where no training data was required for solving the classical inverse problems, e.g., image denoising, inpainting and super-resolution. To introduce DIP in a concise manner, we first consider the most basic reconstruction problem: supposing x_0 is a noisy image, we want to find the unknown clean image x, which can be setup as the following optimization problem

$$\hat{x} = \arg\min_{x} \left\{ \|x - x_0\|^2 + \lambda R(x) \right\}. \tag{3}$$

Here, $R(x)$ is the regularization term, and the weighting parameter $\lambda > 0$ controls the strength of regularization.

Rather than directly solving the optimization in (3) with explicit regularization $R(x)$, the DIP framework offers an alternative way to implicitly regularize the denoising problem and to realize the estimation of $\hat{x}$ by using the optimized network weights. More precisely, DIP ignores the explicit regularization term $R(x)$ in (3) and imposes the reparametrization $x = f_\theta(z)$ as a constraint to the optimization problem (3). Here, f is a deep generative network (e.g., U-Net), which takes random noise z as input and randomly initialized θ as weights. Then, the associated optimization for DIP can be formulated as

$$\hat{\theta} = \arg\min_{\theta} \|f_\theta(z) - x_0\|^2, \quad \hat{x} = f_{\hat{\theta}}(z), \tag{4}$$

where $\hat{x}$ is the final denoised image. Since the network f is not pre-trained from data in any aspects, such deep image prior, like the classical total variation method, is effectively handcrafted. Results in the original DIP article [6] and the recent articles [11], [30], [31] demonstrated that the network architecture can function as an implicit optimized regularizer.

B. Proposed DeepEIT Framework

As we mentioned in Section II, the FEM is used for solving the forward problem in this work. In this sense, the conductivity distribution σ is associated with the finite element discretization of the measurement domain Ω, i.e., $\sigma \in \mathbb{R}^N$, N is the number of FE nodes. In practice, the domain Ω is usually not a square or rectangular in shape, i.e., σ cannot be reshaped as a square or rectangular matrix directly. To deal with this issue, we define a mapping P between the measurement domain Ω and the image domain, which is always a rectangle/square. By applying the mapping P and recalling the DIP framework discussed in the previous subsection, we represent the conductivity distribution σ as

$$\sigma = P(f_\theta(z)). \tag{5}$$

When substituting σ with the NN in (5), the minimization problem in (2) can be rewritten as

$$\hat{\theta} = \arg\min_{\theta} \|V - U(P(f_\theta(z)))\|^2, \quad \hat{\sigma} = P(f_{\hat{\theta}}(z)). \tag{6}$$

By relying on the FE solver, the optimization in (6) is similar to training deep learning models and one can apply any standard optimization algorithms, e.g., we use Adam optimizer [32] in this study. Fig. 1 illustrates the flowchart of the proposed method in this article.

Next, we present the gradient calculation for the measurement data to perform Adam optimization. For easy description, we define the loss function as $L = \|V - U(\sigma)\|^2$. Then, the gradient of the loss function L with respect to the NN parameters θ can be obtained as

$$\frac{\partial L}{\partial \theta} = \left(\frac{\partial L}{\partial \sigma}\right)^T \frac{\partial \sigma}{\partial \theta}. \tag{7}$$

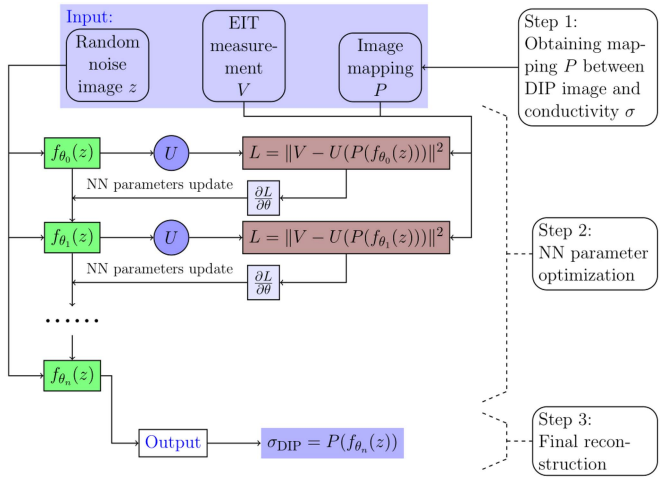

Fig. 1. Flowchart of the DIP based EIT reconstruction method.

Algorithm 1: DeepEIT: DIP-Based EIT Reconstruction Method.

1: Initialization and input: NN input σ_{in}, NN parameters θ, pre-setting auxiliary variables $\theta_{\text{pre}} = \theta$, learning rate lr, $L_{\text{pre}} = inf$, threshold ϵ, measured voltages V, image mapping P and max-iterations.
2: **repeat**
3: $\sigma_{\text{out}} = NN(\sigma_{\text{in}}; \theta)$
4: $U = U(P(\sigma_{\text{out}}))$
5: Compute $L = \|V - U\|^2$
6: **if** $(L - L_{\text{pre}})/L > \epsilon$ **then** ▷ Loss Stabilization Procedure (LSP)
7: $\sigma_{\text{in}} \leftarrow \sigma_{\text{pre}}$, $\theta \leftarrow \theta_{\text{pre}}$, repeat lines 3-5
8: **end if**
9: Compute $\frac{\partial L}{\partial \sigma_{\text{out}}} = 2(\frac{\partial U}{\partial \sigma_{\text{out}}})^T(U - V)$
10: Compute $\frac{\partial L}{\partial \theta} = (\frac{\partial L}{\partial \sigma_{\text{out}}})^T \frac{\partial \sigma_{\text{out}}}{\partial \theta}$
11: Update $\sigma_{\text{pre}} \leftarrow \sigma_{\text{out}}$, $L_{\text{pre}} \leftarrow L$ and $\theta_{\text{pre}} \leftarrow \theta$,
12: Update θ using Adam optimizer
13: **until** max-iterations

The first term $\frac{\partial L}{\partial \sigma}$ can be derived from the loss function

$$\frac{\partial L}{\partial \sigma} = 2\left(\frac{\partial U}{\partial \sigma}\right)^T (U - V). \tag{8}$$

Here, the so-called standard method [33], [34] is applied for calculating the gradient term $\frac{\partial U}{\partial \sigma}$. The second term $\frac{\partial \sigma}{\partial \theta}$ in (7) can be computed automatically via back-propagation with the built-in differentiation engine called *torch.autograd* in PyTorch, since σ is obtained by multiplying the mapping matrix (the linear map P) with the NN output $f_\theta(z)$.

To describe the distinct steps of the proposed approach, in the following subsection, we provide the Pseudo code related to the implementation of the proposed approach.

C. Pseudo-Code

The pseudo-code of the proposed DeepEIT framework is shown in Algorithm 1.

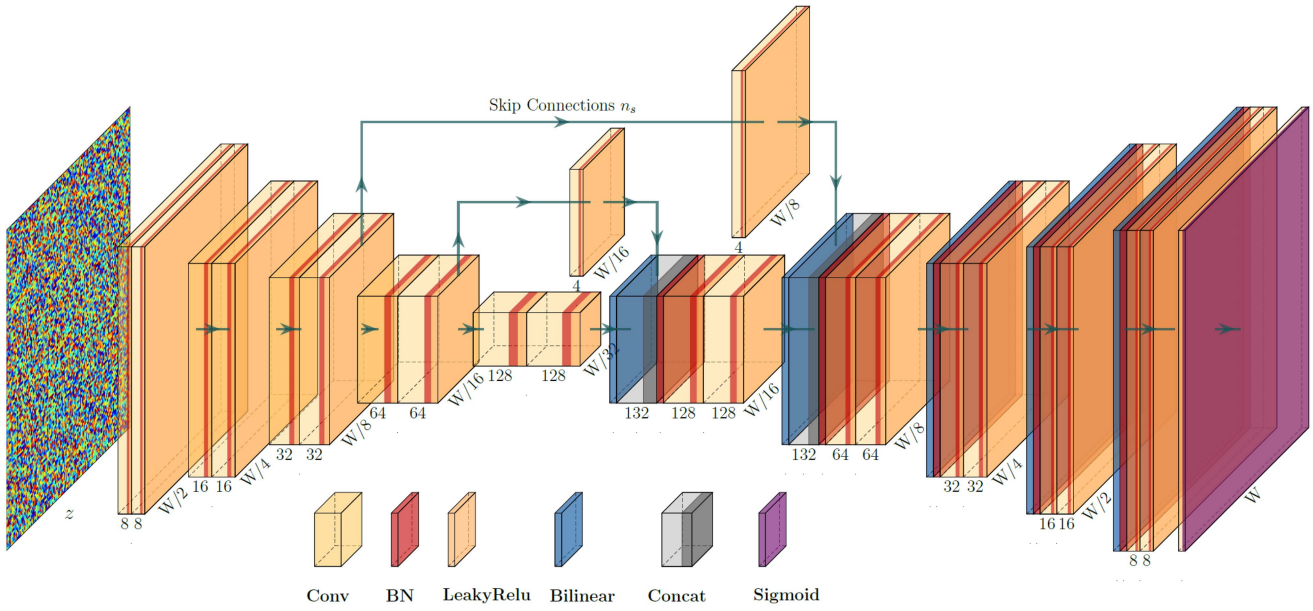

Fig. 2. Neural network architecture. The architecture is based on the popular U-net with skip connections $n_s = [0, 0, 0, 4, 4]$ between the down-sampling layers and up-sampling layers.

IV. Methods

In this section, we detail important components of the experimental investigation, where we study the efficacy of the proposed method with numerical and experimental data. We begin by describing the neural network used for solving the image reconstruction problem. Following, we discuss the test cases and finite element information used in evaluating the proposed method. Lastly, we provide the evaluation criteria and details relevant to implementing the proposed method.

A. Neural Network Architecture

In the original DIP work [6], several architectures were considered for different applications, e.g., encoder–decoder for image denoising. In this work, we employ the same encoder-decoder architecture as in [6] with skip-connections, e.g., $n_s = [0, 0, 0, 4, 4]$ for each skip layer. Here, the non-zero element in the vector n_s denotes the channel number of the convolution kernel in the skip connections, and the zero element of the vector n_s means that there is no skip connection in the particular layer. Generally, skip connections are used to enable feature re-usability and stabilize training and convergence [35]. Hence, the encoder-decoder architecture may use the fine-grained features learned in the encoder part to construct an image in the decoder part. During the encoding process, common stride is used as the down-sampling technique. Bi-linear up-sampling is chosen as the up-sampling operation in the decoding process. The input is a random noise image z, and the output image $f_\theta(z)$ is used to represent the conductivity distribution. In other words, we use neural network to parameterize the conductivity distribution, and the final conductivity distribution is obtained by optimizing the parameters of neural network instead of optimizing the conductivity directly like the traditional iterative methods. The neural network architecture is illustrated in Fig. 2.

LeakyReLU is used as the activation function in the hidden layer. Considering that the conductivity is physically larger than 0, we use the activation function (sigmoid) to convert the NN output into conductivity values in the last layer. Since the output of sigmoid functions varies between 0 and 1, to obtain conductivity value bigger than 1, we multiply the activation sigmoid function by a coefficient $\eta\sigma_{\text{hom}}$. Here, η is a user-defined positive value, and $\sigma_{\text{hom}} \in \mathbb{R}$ is the best homogeneous estimate

$$\sigma_{\text{hom}} = \arg\min \left\{ \|V - U(\sigma)\|^2 \right\}. \tag{9}$$

Finally, the input noise image z is generated by the uniform distribution $z \sim U(0, \frac{1}{10})$, and its size is same as the output size, which is $1 \times W \times H$, where W and H are both set to 128 in this study. The convolution kernel size is set as 3×3 (1×1 for skip-connections). We adopt the Adam optimizer to optimize the NN parameters with a learning rate $lr = 0.001$. Optimization terminates when the maximum number of iterations reaches 5000 and 2000 for simulated data and water tank data, respectively. In this study, all the experiments are implemented in Windows PyTorch 1.10 using custom Python code[2] on a desktop pc with an Intel i7-11700 CPU @ 3.60 GHz and 32 GB of RAM.

We remark that the skip connections n_s and the learning rate lr were fixed for all the experimental studies, except in the ablation and robustness studies of the proposed approach with respect to different hyperparameters (see details in Section VI).

B. Test Cases and Finite Element Information

In the numerical study, a disk with a 14 cm radius was used as the measurement domain. Sixteen electrodes with width 2.5 cm were set equidistantly on the boundary. Electric currents with

[2]To facilitate model reuse, the code that support the findings of this study are available from the corresponding author upon reasonable request.

TABLE I
PERFORMANCE METRICS OF SIMULATION AND EXPERIMENTAL STUDIES

	Case 1				Case 2				Case 3				Case 4				Case 5			
	SSIM	CC	PSNR	RE	SSIM	CC	PSNR	RE	SSIM	CC	PSNR	RE	SSIM	CC	PSNR	RE	SSIM	CC	PSNR	RE
DIP	**0.87**	**0.96**	**23.0**	**0.016**	**0.90**	**0.85**	**20.6**	0.015	**0.79**	**0.82**	16.6	0.039	**0.81**	**0.84**	**17.0**	**0.029**	**0.69**	**0.73**	13.5	0.082
NOSER	0.47	0.88	11.3	0.241	0.82	0.62	16.1	0.041	0.65	0.59	13.0	0.091	0.67	0.61	12.7	0.079	0.55	0.54	11.0	0.145
L_2	0.73	0.92	20.3	0.030	0.88	0.80	19.9	0.017	0.74	0.79	**16.9**	**0.037**	0.74	0.78	15.9	0.038	0.62	**0.73**	**14.2**	**0.070**
TV	0.77	0.90	19.2	0.038	0.87	0.85	**20.6**	**0.014**	0.73	0.75	15.8	0.048	0.77	0.79	16.0	0.037	0.65	0.72	14.0	0.074

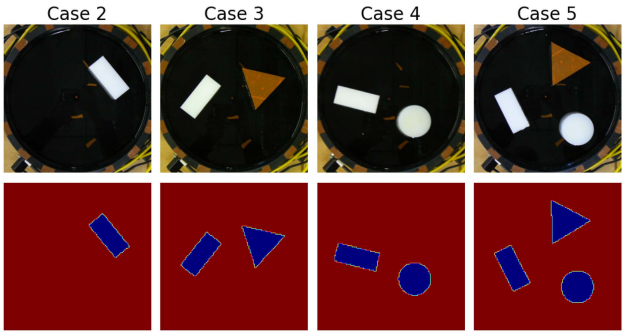

Fig. 3. Examples of target photographs and masks that are used to generate the inclusion conductivity distribution for computing the performance metrics.

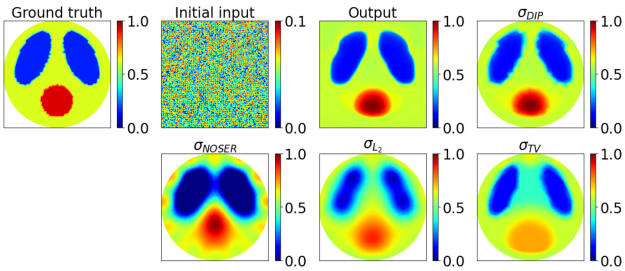

Fig. 4. Case 1: results of the simulated heart-and-lungs phantom. Initial input: random noise image z; Output: $f_{\hat{\theta}}(z)$; σ_{DIP}: DeepEIT based reconstruction, i.e., $\sigma_{DIP} = P(f_{\hat{\theta}}(z))$. σ_{NOSER}: NOSER based reconstruction; σ_{L_2} and σ_{TV}: reference estimations using smoothness prior and total variation, respectively.

an amplitude of 1 mA were injected into the measurement domain. The current stimulation and voltage measurement are based on adjacent patterns. The conductivities of the tissues were respectively set as 0.25 mS/cm for the lungs, 1 mS/cm for the background and 1.5 mS/cm for the heart. The simulated measurements were computed with 2-D FE simulations using a first order mesh with $N_n = 3154$ nodes and $N_e = 6130$ elements. To avoid the so-called 'inverse crime,' a first order mesh with $N_n = 484$ nodes and $N_e = 902$ elements was used as the inverse mesh. To simulate real conditions, Gaussian noise of SNR=60 dB was added to the simulated noiseless measurements. Our numerical study, denoted as Case 1, deals with a simulated heart-and-lungs phantom, as shown in Fig. 4.

The experimental data was collected with the KIT-4 measurement system [36] using a saline tank phantom. The phantom had a 14 cm radius and 7 cm height and was equipped with 16 equally distanced electrodes. The frequency of the injected current was set to 10 kHz and the amplitude was 1 mA, and adjacent measurement patterns were used in the measurements. As shown in Fig. 3, four different targets denoted as Cases 2-5 were constructed by inserting non-conductive objects with different shapes into the tank. During the reconstruction, the same inverse mesh as in the simulation study was applied.

C. Implementation Details

To quantitatively test the reconstruction performances, as shown in Table I, we computed the correlation coefficient (CC), the peak signal-to-noise ratio (PSNR) and relative error (RE) of the estimated conductivity. Meanwhile, we utilized the structural similarity index (SSIM) for measuring the similarity between the true conductivity and reconstructed images. An SSIM value of 1 refers to a perfect match between the reconstructed image and the original one. Since the true conductivity for the experimental test cases is not accessible, we artificially assigned a conductivity distribution based on the target photograph and the corresponding mask, as shown in Fig. 3, for computing performance metrics. It should be emphasized that this artificially assigned conductivity and the mask are, fundamentally, *not* required for implementing the proposed approach.

During the optimization process, destabilization is observed as significant loss increase and degeneration in the generated image $f_{\hat{\theta}}(z)$. To avoid such destabilization, we simply imposed a Loss Stabilization Procedure (LSP) to track the loss value and return to the parameters corresponding to the previous iteration if $(\text{Loss}_i - \text{Loss}_{i-1})/\text{Loss}_i$ is higher than a certain threshold $\epsilon = 0.01$. The effect to the proposed method with and without LSP will be studied in Section VI.

To facilitate ease of visual comparison, the results presented in this work are scaled using Min-Max normalization to bring all values into the range $[0, 1]$. Due to the fact that the reference NOSER is a difference imaging approach, it estimates the conductivity change $\delta\sigma$. We simply added σ_{hom} to form the conductivity $\sigma_{\text{NOSER}} = \delta\sigma + \sigma_{\text{hom}}$.

V. RESULTS

In this section, we show the results of the numerical and experimental studies. To check the performance of the proposed DeepEIT framework, we also computed conventional reconstructions based on smoothness prior [37] and total variation prior [38], as well as the NOSER based reconstruction [39]. Since DeepEIT is learned without data training, we omit the reconstructions based on trained CNNs from our analysis. For more recent and general expositions on applying trained CNNs and shape-driven approaches in EIT with similar experimental data, we refer the reader to [19], [21], [40], [41], [42].

A. Simulation Results

Fig. 4 depicts the results of the simulated heart-and-lungs phantom. We observe that the image quality of the proposed

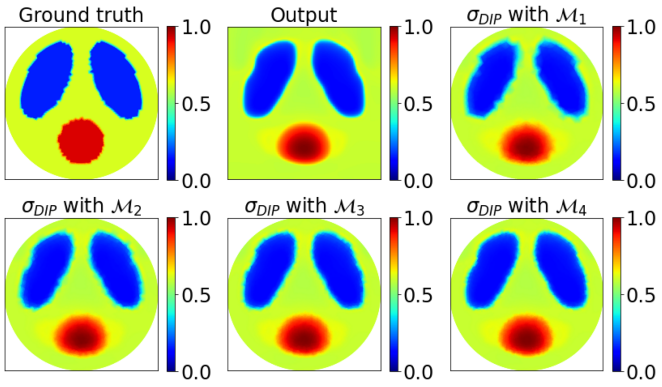

Fig. 5. High resolution boundary extraction by mapping the output $f_{\hat{\theta}}(z)$ into meshes $\mathcal{M}_i$, $i \geq 1$ is the mesh density level, the larger the level the finer the mesh.

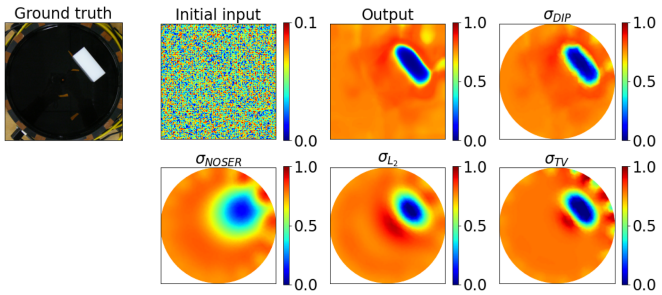

Fig. 6. Case 2: experimental study with a rectangle target. Otherwise as in Fig. 4.

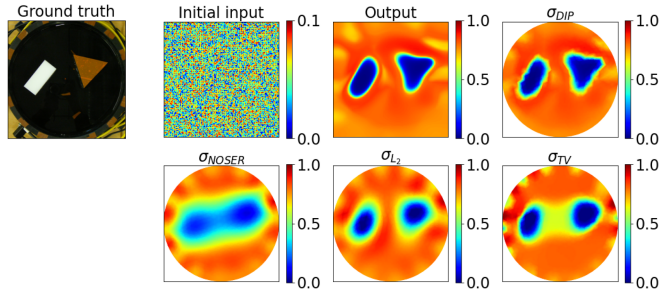

Fig. 7. Case 3: experimental study with one rectangular target and one triangular target. Otherwise as in Fig. 4.

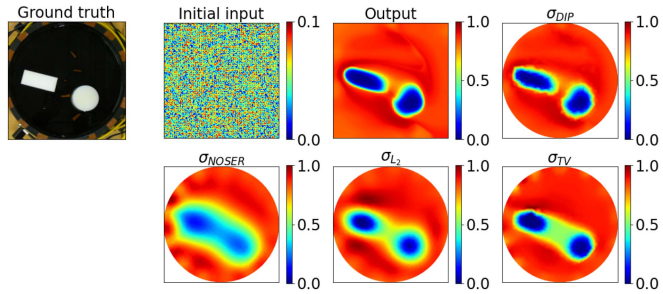

Fig. 8. Case 4: experimental study with one rectangular target and one cylindrical bar target. Otherwise as in Fig. 4.

method is visibly superior to quality of the reference methods, which is also confirmed by the evaluation criteria SSIM and CC, as tabulated in Table I. Meanwhile, the proposed method leads to an almost clean image with virtually no obvious artifacts, while for the referenced methods significant artifacts remain visible in the domain. Especially, the blurred/staircase effect induced by reference methods makes it difficult to track a clear interface between the target and the background.

In fact, obtaining high resolution boundaries is one of the key challenges in EIT. Traditionally, this is often achieved by employing shape-driven schemes [40], [43], [44], or by incorporating the patient specific structure information (e.g., CT data) in the reconstruction process [45]. However, these schemes require strong and precisely quantified prior knowledge about the specific object, which may not be accessible in real applications or expensive to obtain. In the proposed framework, one can extract a high resolution boundary without additional cost as follows. First, running the DeepEIT optimization with a coarse mesh (denoted as $\mathcal{M}_1$); then the NN output $f_{\hat{\theta}}(z)$ can be mapped into any fine mesh (denoted as $\mathcal{M}_{i,i>1}$, i is the mesh density level) for achieving the conductivity distribution at a fine resolution, as illustrated in Fig. 5.

B. Experimental Results

In this subsection, we analyze the performance of the proposed DeepEIT framework using water tank data. The reconstructions are provided in Figs. 6–9. We first present the results of the experiment with one rectangular inclusion, as shown in Fig. 6. It is apparent that location of the inclusion is reliably recovered by all the studied methods. However, the proposed approach and TV based method outperform NOSER and L_2 norm based method for recovering the shape of the rectangular-shaped inclusion. Indeed, σ_{NOSER} and σ_{L_2} provide deformed shape reconstruction with blurred properties, which is caused by the smoothness prompting regularization applied in both methods.

Visually, artifacts along the domain boundary presented in all the reconstructions. This is mainly due to the following aspects: 1) the modeling uncertainties (e.g., modeling errors caused by unknown contact impedance and position mismatch between the real electrode and modeled one, and measurement noise) accompanied in the reconstruction, which may propagate during the reconstructions; 2) the observation model used in this study is based on the context of absolute imaging, which is known to be sensitive to such uncertainties, and 3) the hyper-parameters for all the methods are empirically selected based on trial-and-error method and kept the same for all the study cases, i.e., no individual tuning was performed for each case. This may not be optimal. Since we are focusing on studying the performance of the proposed DeepEIT, we defer the possible solutions to address these challenges in the future works.

Next, we present the reconstructions of the test (Cases 3&4) considering two inclusions. Upon first visual inspection of inclusions in Figs. 7 and 8, it is immediately apparent that, for NOSER, the reconstructed inclusions are visually almost indistinguishable. For TV, the undesirable staircase effect exists and makes it difficult to track the boundary details. L_2 norm based reconstruction introduces severe blurry artifacts which lead to unwanted features (e.g., shape distortions) and less

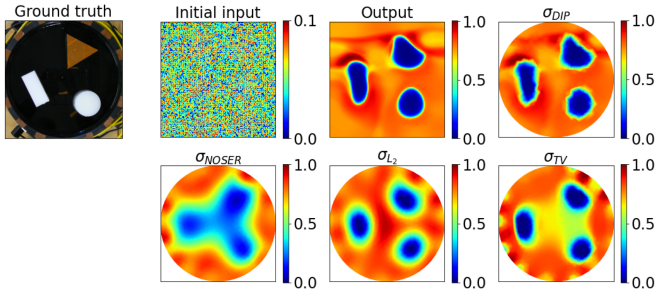

Fig. 9. Case 5: experimental study with three targets. Otherwise as in Fig. 4.

faithful results when compared to the original inclusions. On the other hand, the proposed method is visibly superior to the quality of the reference estimates, leading to the best criteria SSIM and CC in both cases. Especially, the shape details are fairly well recovered, e.g., the triangular shape of the inclusion in Case 3 of Fig. 7. In fact, recovering shape details (e.g., sharp corners in the triangular-shaped inclusion) without structural information is a notoriously challenging task in EIT.

Finally, we report the results of Case 5, conducted with three inclusions, as shown in Fig. 9. Once again, visually, the positions of the inclusions correspond to the real targets for all the methods. The proposed method performs fairly well in recovering major shape characteristics, achieving the best SSIM and CC parameters among the reference methods. This is consistent with the findings of the previous numerical simulation and experimental studies.

As a whole, it can be concluded that the proposed DIP-based approach results in dramatically improved estimations compared to the (tested) traditional regularization based methods. The difference is particularly remarkable for experimental cases with triangular-shaped inclusions, where the proposed method produces more informative inversions.

VI. Discussion: Opportunities, Challenges and Robustness

In this section, we will discuss the current challenges and robustness issues related to applying DIP in EIT. Additionally, potential opportunities are also identified in the context of these challenges and problems.

A. Efficiency

Since our DeepEIT framework falls into the category of model-driven learning approaches [46], iterations are essentially required for optimizing the NN parameters. Also, the current work is formulated in the context of absolute imaging framework, i.e., it requires repeated solving of the forward problem, which is known to be computationally expensive. Taking Case 1 as an example, the number of trainable parameters θ in the network is about 0.57 millions and 2.30 MB storage is required for saving these parameters. The total computational time for 5000 iterations is 5172 seconds, i.e., the average computational cost is about 1.03 seconds per iteration. For these reasons, the current proposed approach results in lack of efficiency, which is a major obstacle to directly apply it in real-world applications. Further work is required in order to improve this scheme:

- Formulating DeepEIT in context of difference imaging through a linearization to the observation model, which is known to speed up reconstruction and circumvent highly-accurate modelling requirements [44];
- Integrating traditional methods when designing the networks, e.g., using a reference image as the input to speed up convergence;
- Starting the training process by transferring the weights from the pre-training models [47], [48], instead of training from scratch, and
- Applying the so-called ADMM optimizer to decouple the NN training step and conductivity updating step [10], as computing the EIT forward problem is time consuming. This concern is related to the fact that NN training needs more steps than updating the conductivity.

B. Integration With Explicit Regularization or Prior Information

Extending the DeepEIT framework by combining it with an explicit regularization or prior information offers great potential to enrich the overall regularization effect and to stabilize the reconstruction [31]. For example, the traditional TV regularization and structural prior information could be merged into the optimization model in order to achieve better image recovery. In addition to incorporating prior knowledge on the image domain, i.e., the conductivity distribution, one may also consider to integrate learned regularization techniques [49] to regularize the NN parameters throughout the optimization process. A more in-depth investigation should be focused on studying the implicit regularization effect that DIP brings. Such a feature may help in integrating a complementary explicit regularization via the minimization problem (6), thereby getting a stronger effect and better performance.

Inspired by the successful improvement of DIP framework with explicit regularization [30], [31], [50], we further briefly showcase the comparison study of the proposed DIP framework with and without (isotropic) TV regularization [51]. Mathematically, an explicit term is added into the minimization problem in (6) to form the framework of DIP+TV, i.e.,

$$\hat{\theta} = \arg\min_{\theta} \left\{ \|V - U(P(f_\theta(z)))\|^2 + \lambda \mathrm{TV}(f_\theta(z)) \right\}. \quad (10)$$

Here, the weighting parameter λ is selected as 1×10^{-3}, and the TV functional is of the form

$$\mathrm{TV}(m) = \sum_{i,j} \sqrt{(m_{i+1,j} - m_{i,j})^2 + (m_{i,j+1} - m_{i,j})^2 + \beta}, \quad (11)$$

where $\beta = 1 \times 10^{-10}$ is a small parameter which ensures that the TV functional is differentiable.

Fig. 10 depicts that DIP+TV outperforms original DIP and leads to considerable performance gains on preserving the conductivity profiles (e.g., sharpness) and eliminating the background artifacts, as evident from the performance metrics marked below the Fig. 10. This is a reasonable result given

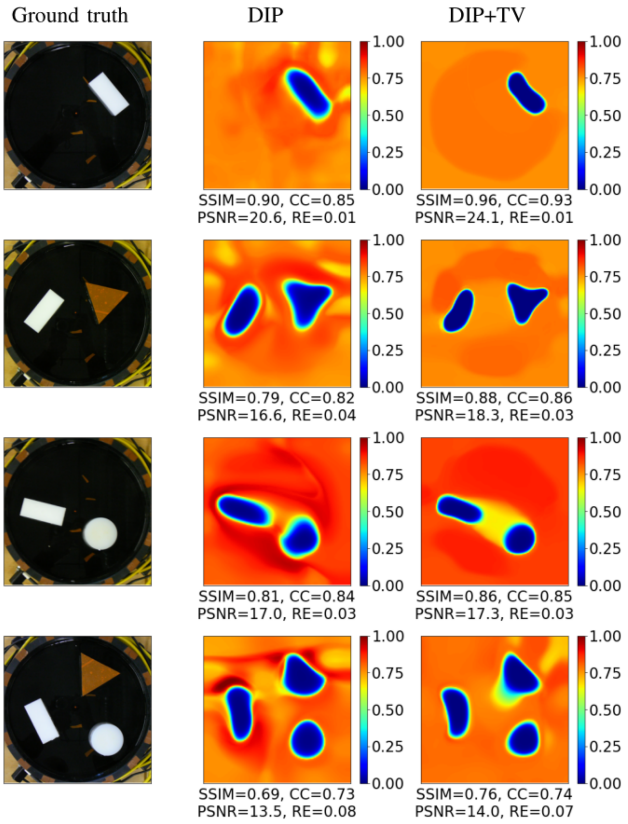

Fig. 10. Comparison of the proposed DeepEIT framework with and without explicit TV regularization.

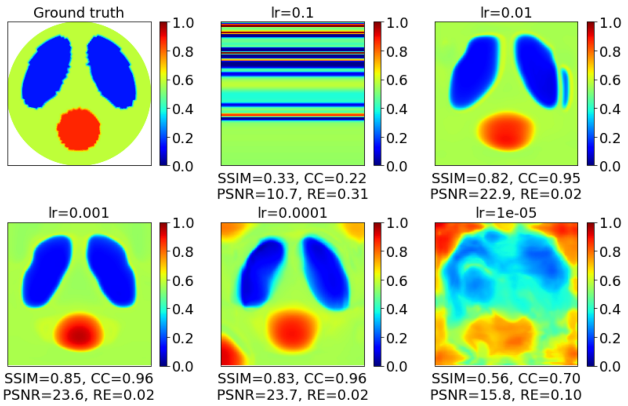

Fig. 11. Robustness study of the proposed DeepEIT framework using different learning rate.

that the phantom is piecewise constant. This behavior can be explained by the fact that TV induces additional ability of sparsity prompting to the DIP framework, which is consistent to the previous study [50] in traditional restoration tasks such as image denoising and deblurring. It is worth remarking that DIP+TV suffers from undesired staircase artifacts, which are typical of TV reconstructions. To overcome this shortcoming, one may consider updating the optimization model by combining with the total generalized variation [52] regularization for preserving the fine detail and minimizing the staircase effect. However, in this article, we mainly focus on developing the

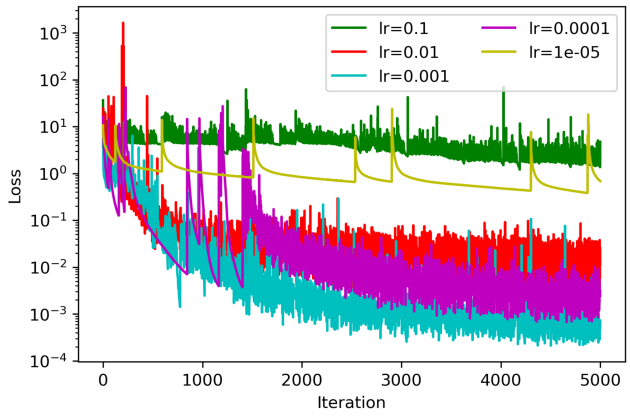

Fig. 12. Loss curves of Case 1 with five different learning rates.

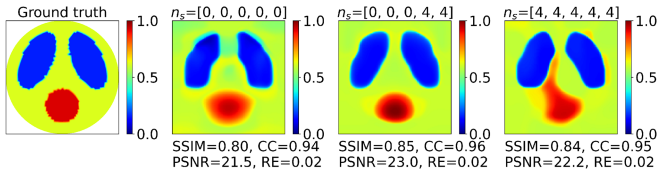

Fig. 13. Ablation study of the proposed DeepEIT framework by varying the skip connections.

DIP framework for EIT and exploring its implicit regularization effect, we defer analyzing the DIP in combination with other explicit regularization to a future work.

C. Hyperparameter Optimization and Ablation Study

In this subsection, we begin by performing a robustness study of the proposed approach with respect to different learning rates. Following, an ablation study for checking the performance of the NN is considered by removing or adding different skip connections. Lastly, we conduct a comparison study for investigating the effect of Loss Stabilization Procedure and early stopping to the DeepEIT framework.

1) Varying Learning Rate: To investigate the effects of the learning rate on model's performance and to build an intuition about the dynamics of the learning rate on model's behavior, we performed a set of DIP reconstructions for Case 1 with learning rate decreasing logarithmically from 0.1 to 1×10^{-5}. From the reconstructions shown in Fig. 11 and the corresponding loss curves shown in Fig. 12, we can easily see the influence of using five different learning rates with the Adam optimizer. The learning rate of $lr = 0.001$ outperforms the other scenarios, proving that for this case, it is the optimized value. In fact, a learning rate ($lr = 0.1$) that is too large can cause instability and hinder convergence, whereas a learning rate ($lr = 1 \times 10^{-5}$) that is too small can cause the reconstruction process to get stuck. It appears that a learning rate of around 0.01 to 0.0001 seems to provide an appropriate selection for the DeepEIT framework. Note that the learning rate is empirically chosen in this article, there remains a crucial need to incorporate automatic techniques for automatically picking such hyper-parameters. A potential solution, which could be considered, is to apply the population

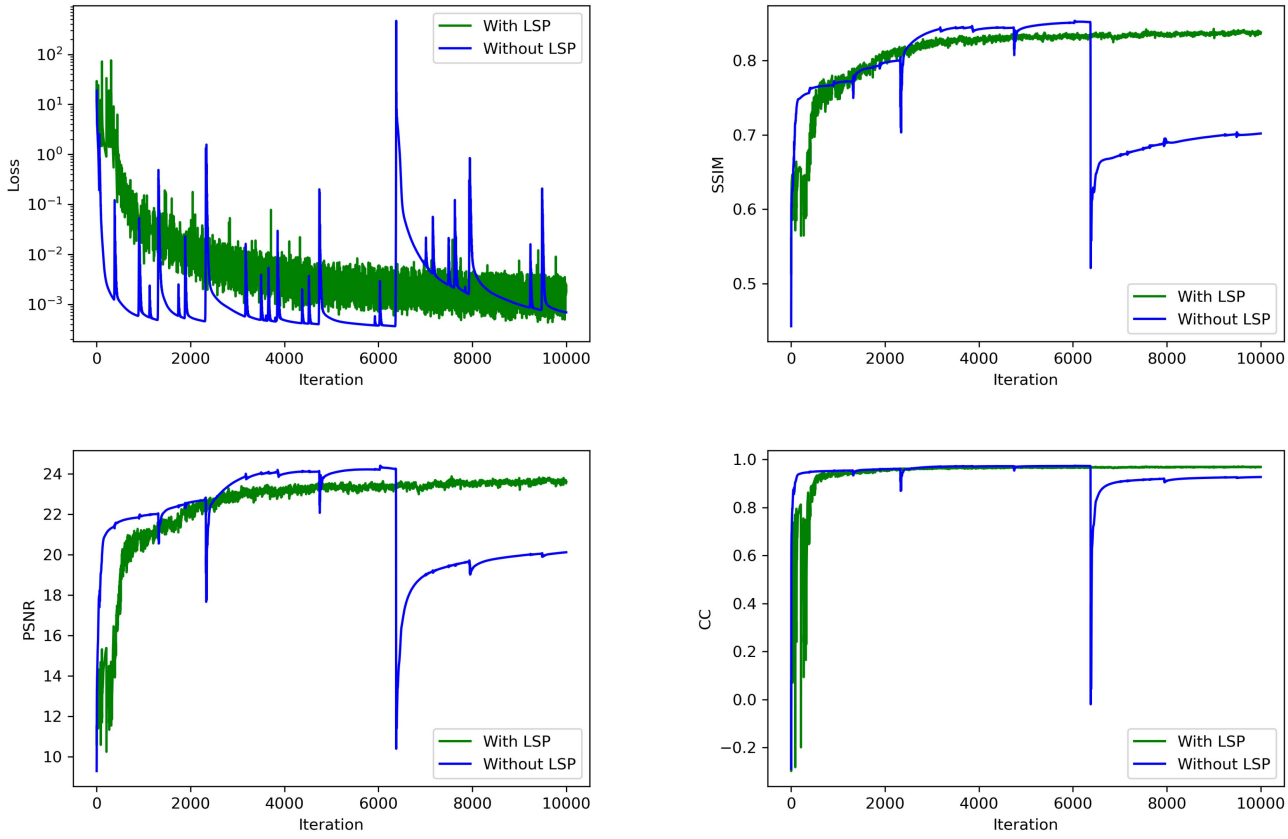

Fig. 14. Curves of loss function and performance metrics over iterations.

based training algorithm developed by DeepMind [53] for finding a flexible solution to the model architecture. We remark that, optimizing the learning rate is out of the scope of this article, hence it was left as a future research.

2) Varying Skip Connections: To check the importance of the skip connections for the training of NN model f_θ and how the proposed approach performs, NN with variant skip connections n_s are constructed and applied for recovering the conductivity profile of Case 1. As depicted in Fig. 13, NN with skip connections $n_s = [0, 0, 0, 4, 4]$ provides the best reconstruction over the other two cases, i.e., NN with $n_s = [0, 0, 0, 0, 0]$ and NN with $n_s = [4, 4, 4, 4, 4]$, leading the best evaluation metrics. We remark that the benefit of adding such a sophisticated skip connections (e.g., $n_s = [0, 0, 0, 4, 4]$) is also significant for avoiding the vanishing gradient problem [54], since skip connections allow the propagation of the gradient flow. It should be emphasized that the skip connections used in the current encoder-decoder architecture is restrictive, demanding the fusion of the same-scale feature maps from the encoder and decoder. In fact, one may also consider to replace the classical U-Net architecture with nested and dense skip connections based U-Net++ [35] when designing the NNs, for obtaining better feature accumulation across the network, both horizontally and vertically.

D. Effect of Loss Stabilization Procedure and Early Stopping

Fig. 14 depicts the loss function and performance metrics during optimization of DIP-regularized reconstructions of Case 1.[3] We observe that the optimization process *without* LSP suffers from numerical instability, e.g., it may diverge rapidly while the loss increases significantly. This trend is also observed in the original DIP article [6] and a recent work in the field of diffraction tomography [55]. On the other hand, numerical instability is much less observed in the LSP augmented DIP-regularized reconstructions. This is mainly because LSP allows to track the optimization loss at each iteration and counteracts the undesired divergence in an automated fashion. The former can be achieved by restoring the NN parameters to the previous iteration if $(\text{Loss}_i - \text{Loss}_{i-1})/\text{Loss}_i$ is higher than the threshold $\epsilon = 0.01$. This comparison study helps demonstrate the individual contributions of LSP to the NNs.

What remains to be discussed is how to reduce overfitting in neural networks. As reported in [6], [56], DIP has a bias toward the desired content, and learns it much faster than learning the noise. This trend is also observed in our DIP-regularized reconstruction without LSP. This result is expected, since estimating parameters in NNs from a single image input poses a huge risk of overfitting, such that the networks' ability for accurate parameter estimation is significantly influenced by early stopping. For example, we found that the reconstruction quality reaches a (local) peak and then induces potentially degradation due to modeling error and noise. To remedy such an overfitting issue, early stopping is usually required. However, how to select an

[3]To evaluate the trends of over-fitting and instability, we iterate the DIP-regularized reconstruction for 10000 steps.

optimal stopping point around the performance peak is still an open question and full of challenges. Fortunately, with the help of LSP, we did not have to employ early stopping to avoid overfitting, since LSP robustifies the reconstruction from the risk of overfitting to some extent. However, we need to emphasize that the early stopping is relevant in LSP augmented DIP reconstructions for saving computational time, since the updates after a certain number of iterations become sufficiently small and one may consider to stop before reaching the final steps.

Lastly, we wish to mention that, from a Bayesian probabilistic perspective [57], [58], the overfitting could also be prevented by incorporating proper priors over the parameters and then quantifying uncertainty with posterior distributions. Future work can further investigate the possibility of fusing Bayesian learning [59], [60], [61] and DIP to better understand the regularization implied by NNs and solve the EIT reconstruction problem.

VII. Conclusion

In this work, we presented a novel deep image prior based framework (DeepEIT) for image reconstruction in EIT. DeepEIT parameterizes the conductivity distribution under reconstruction as the output of a convolutional network with random parameters and a random input. In other words, instead of optimizing the conductivity distribution in the image space, we now optimize it in the space of the neural network's parameters. We emphasize that no training data is utilized in the optimizing neural network's parameters. Essentially, DIP is an appealing model-driven unsupervised learning approach. This work offers a framework to further extend its applications in the field of inverse problems. Our solution relied on the fact that the implicit regularization induced by learning algorithms [62], e.g., convolutional neural networks, makes DIP particularly relevant for image reconstruction. As demonstrated in this article, DeepEIT is a relatively effective machine for handling the EIT reconstruction problem. Therefore, we believe that DeepEIT provides a viable alternative to the existing EIT image reconstructions. More in-depth experimental works exploring the DeepEIT framework are required, and multidisciplinary research in addressing the challenges and opportunities described in Sec. VI will form the basis of future research.

Acknowledgments

The authors would like to thank the inverse problems group at University of Eastern Finland for sharing the respective experimental data sets.

References

[1] L. Lu, X. Wang, G. Carneiro, and L. Yang, *Deep learning and convolutional neural networks for medical imaging and clinical informatics*. Cham, Switzerland: Springer Nature Switzerland AG, 2019.

[2] Y. Zhao, A. Raghuram, H. Kim, A. Hielscher, J. T. Robinson, and A. N. Veeraraghavan, "High resolution, deep imaging using confocal time-of-flight diffuse optical tomography," *IEEE Trans. Pattern Anal. Mach. Intell.*, vol. 43, no. 7, pp. 2206–2219, Jul. 2021.

[3] B. Zhu, J. Z. Liu, S. F. Cauley, B. R. Rosen, and M. S. Rosen, "Image reconstruction by domain-transform manifold learning," *Nature*, vol. 555, no. 7697, pp. 487–492, 2018.

[4] Y. LeCun, Y. Bengio, and G. Hinton, "Deep learning," *Nature*, vol. 521, no. 7553, pp. 436–444, 2015.

[5] G.-J. Qi and J. Luo, "Small data challenges in Big Data era: A survey of recent progress on unsupervised and semi-supervised methods," *IEEE Trans. Pattern Anal. Mach. Intell.*, vol. 44, no. 4, pp. 2168–2187, Apr. 2022.

[6] D. Ulyanov, A. Vedaldi, and V. Lempitsky, "Deep image prior," in *Proc. IEEE Conf. Comput. Vis. Pattern Recognit.*, 2018, pp. 9446–9454.

[7] R. Heckel and M. Soltanolkotabi, "Denoising and regularization via exploiting the structural bias of convolutional generators," 2019, *arXiv: 1910.14634*.

[8] R. Heckel, "Regularizing linear inverse problems with convolutional neural networks," 2019, *arXiv:1907.03100*.

[9] R. Heckel and M. Soltanolkotabi, "Compressive sensing with un-trained neural networks: Gradient descent finds a smooth approximation," in *Proc. Int. Conf. Mach. Learn.*. PMLR, 2020, pp. 4149–4158.

[10] K. Gong, C. Catana, J. Qi, and Q. Li, "PET image reconstruction using deep image prior," *IEEE Trans. Med. Imag.*, vol. 38, no. 7, pp. 1655–1665, Jul. 2019.

[11] D. O. Baguer, J. Leuschner, and M. Schmidt, "Computed tomography reconstruction using deep image prior and learned reconstruction methods," *Inverse Problems*, vol. 36, no. 9, 2020, Art. no. 094004.

[12] J. Yoo, K. H. Jin, H. Gupta, J. Yerly, M. Stuber, and M. Unser, "Time-dependent deep image prior for dynamic MRI," *IEEE Trans. Med. Imag.*, vol. 40, no. 12, pp. 3337–3348, Dec. 2021.

[13] M. Mozumder, A. Hauptmann, I. Nissilä, S. R. Arridge, and T. Tarvainen, "A model-based iterative learning approach for diffuse optical tomography," *IEEE Trans. Med. Imag.*, vol. 41, no. 5, pp. 1289–1299, May 2021.

[14] A. Romanowski, "Big data-driven contextual processing methods for electrical capacitance tomography," *IEEE Trans. Ind. Informat.*, vol. 15, no. 3, pp. 1609–1618, Mar. 2019.

[15] R. Bayford, R. Sadleir, and I. Frerichs, "Advances in electrical impedance tomography and bioimpedance including applications in covid-19 diagnosis and treatment," *Physiol. Meas.*, vol. 43, no. 2, 2022, Art. no. 020401.

[16] L. Eichler, J. Mueller, J. Grensemann, I. Frerichs, C. Zöllner, and S. Kluge, "Lung aeration and ventilation after percutaneous tracheotomy measured by electrical impedance tomography in non-hypoxemic critically ill patients: A prospective observational study," *Ann. Intensive Care*, vol. 8, no. 1, 2018, Art. no. 110.

[17] T. Mauri et al., "Potential for lung recruitment and ventilation-perfusion mismatch in patients with the acute respiratory distress syndrome from Coronavirus disease 2019," *Crit. Care Med.*, vol. 48, no. 8, 2020, Art. no. 1129.

[18] S. Hannan, K. Aristovich, M. Faulkner, J. Avery, M. C. Walker, and D. S. Holder, "Imaging slow brain activity during neocortical and hippocampal epileptiform events with electrical impedance tomography," *Physiol. Meas.*, vol. 42, no. 1, 2021, Art. no. 014001.

[19] S. J. Hamilton and A. Hauptmann, "Deep D-bar: Real time electrical impedance tomography imaging with deep neural networks," *IEEE Trans. Med. Imag.*, vol. 37, no. 10, pp. 2367–2377, Oct. 2018.

[20] M. Capps and J. L. Mueller, "Reconstruction of organ boundaries with deep learning in the D-bar method for electrical impedance tomography," *IEEE Trans. Biomed. Eng.*, vol. 68, no. 3, pp. 826–833, Mar. 2021.

[21] Z. Wei, D. Liu, and X. Chen, "Dominant-current deep learning scheme for electrical impedance tomography," *IEEE Trans. Biomed. Eng.*, vol. 66, no. 9, pp. 2546–2555, Sep. 2019.

[22] C. Tan, S. Lv, F. Dong, and M. Takei, "Image reconstruction based on convolutional neural network for electrical resistance tomography," *IEEE Sensors J.*, vol. 19, no. 1, pp. 196–204, Jan. 2019.

[23] J. K. Seo, K. C. Kim, A. Jargal, K. Lee, and B. Harrach, "A learning-based method for solving ill-posed nonlinear inverse problems: A simulation study of lung eit," *SIAM J. Imag. Sci.*, vol. 12, no. 3, pp. 1275–1295, 2019.

[24] Y. Chen, K. Li, and Y. Han, "Electrical resistance tomography with conditional generative adversarial networks," *Meas. Sci. Technol.*, vol. 31, no. 5, 2020, Art. no. 055401.

[25] X. Chen et al., "Deep autoencoder imaging method for electrical impedance tomography," *IEEE Trans. Instrum. Meas.*, vol. 70, pp. 1–15, 2021.

[26] Z. Liu, P. Bagnaninchi, and Y. Yang, "Impedance-optical dual-modal cell culture imaging with learning-based information fusion," *IEEE Trans. Med. Imag.*, vol. 41, no. 4, pp. 983–996, Apr. 2021.

[27] K. S. Cheng, D. Isaacson, J. C. Newell, and D. G. Gisser, "Electrode models for electric current computed tomography," *IEEE Trans. Biomed. Eng.*, vol. 36, no. 9, pp. 918–924, Sep. 1989.

[28] P. Vauhkonen, M. Vauhkonen, T. Savolainen, and J. Kaipio, "Three-dimensional electrical impedance tomography based on the complete electrode model," *IEEE Trans. Biomed. Eng.*, vol. 46, pp. 1150–1160, Sep. 1999.
[29] G. González, J. Huttunen, V. Kolehmainen, A. Seppänen, and M. Vauhkonen, "Experimental evaluation of 3D electrical impedance tomography with total variation prior," *Inverse Problems Sci. Eng.*, vol. 24, no. 8, pp. 1411–1431, 2016.
[30] G. Mataev, P. Milanfar, and M. Elad, "DeepRED: Deep image prior powered by red," in *Proc. IEEE/CVF Int. Conf. Comput. Vis. Workshops*, 2019.
[31] S. Dittmer, T. Kluth, P. Maass, and D. OteroBaguer, "Regularization by architecture: A deep prior approach for inverse problems," *J. Math. Imag. Vis.*, vol. 62, no. 3, pp. 456–470, 2020.
[32] D. P. Kingma and J. Ba, "ADAM: A method for stochastic optimization," 2014, *arXiv:1412.6980*.
[33] T. J. Yorkey, J. G. Webster, and W. J. Tompkins, "Comparing reconstruction algorithms for electrical impedance tomography," *IEEE Trans. Biomed. Eng.*, vol. BME-34, no. 11, pp. 843–852, Nov. 1987.
[34] M. Vauhkonen, D. Vadasz, P. A. Karjalainen, E. Somersalo, and J. P. Kaipio, "Tikhonov regularization and prior information in electrical impedance tomography," *IEEE Trans. Med. Imag.*, vol. 17, no. 2, pp. 285–293, Apr. 1998.
[35] Z. Zhou, M. M. R. Siddiquee, N. Tajbakhsh, and J. Liang, "UNet++ : Redesigning skip connections to exploit multiscale features in image segmentation," *IEEE Trans. Med. Imag.*, vol. 39, no. 6, pp. 1856–1867, Jun. 2020.
[36] J. Kourunen, T. Savolainen, A. Lehikoinen, M. Vauhkonen, and L. Heikkinen, "Suitability of a PXI platform for an electrical impedance tomography system," *Meas. Sci. Technol.*, vol. 20, no. 1, 2009, Art. no. 015503.
[37] D. Liu and J. Du, "A moving morphable components based shape reconstruction framework for electrical impedance tomography," *IEEE Trans. Med. Imag.*, vol. 38, no. 12, pp. 2937–2948, Dec. 2019.
[38] Z. Zhou et al., "Comparison of total variation algorithms for electrical impedance tomography," *Physiol. Meas.*, vol. 36, no. 6, 2015, Art. no. 1193.
[39] M. Cheney, D. Isaacson, J. C. Newell, S. Simske, and J. Goble, "NOSER: An algorithm for solving the inverse conductivity problem," *Int. J. Imag. Syst. Technol.*, vol. 2, no. 2, pp. 66–75, 1990.
[40] D. Liu, A. K. Khambampati, and J. Du, "A parametric level set method for electrical impedance tomography," *IEEE Trans. Med. Imag.*, vol. 37, no. 2, pp. 451–460, Feb. 2018.
[41] D. Liu, D. Gu, D. Smyl, A. K. Khambampati, J. Deng, and J. Du, "Shape-driven EIT reconstruction using fourier representations," *IEEE Trans. Med. Imag.*, vol. 40, no. 2, pp. 481–490, Feb. 2021.
[42] D. Liu, D. Gu, D. Smyl, J. Deng, and J. Du, "B-spline level set method for shape reconstruction in electrical impedance tomography," *IEEE Trans. Med. Imag.*, vol. 39, no. 6, pp. 1917–1929, Jun. 2020.
[43] D. Liu and J. Du, "Shape and topology optimization in electrical impedance tomography via moving morphable components method," *Struct. Multidisciplinary Optim.*, vol. 64, no. 2, pp. 585–598, 2021.
[44] D. Liu, D. Gu, D. Smyl, J. Deng, and J. Du, "Shape reconstruction using Boolean operations in electrical impedance tomography," *IEEE Trans. Med. Imag.*, vol. 39, no. 9, pp. 2954–2964, Sep. 2020.
[45] B. Schullcke, B. Gong, S. Krueger-Ziolek, M. Soleimani, U. Mueller-Lisse, and K. Moeller, "Structural-functional lung imaging using a combined CT-EIT and a discrete cosine transformation reconstruction method," *Sci. Rep.*, vol. 6, no. 1, pp. 1–12, 2016.
[46] Z. Xu and J. Sun, "Model-driven deep-learning," *Nat. Sci. Rev.*, vol. 5, no. 1, pp. 22–24, 2018.
[47] S. J. Pan and Q. Yang, "A survey on transfer learning," *IEEE Trans. Knowl. Data Eng.*, vol. 22, no. 10, pp. 1345–1359, Oct. 2009.
[48] T.-A. Song, F. Yang, and J. Dutta, "Noise2Void: Unsupervised denoising of PET images," *Phys. Med. Biol.*, vol. 66, no. 21, 2021, Art. no. 214002.
[49] D. Van Veen, A. Jalal, M. Soltanolkotabi, E. Price, S. Vishwanath, and A. G. Dimakis, "Compressed sensing with deep image prior and learned regularization," 2018, *arXiv:1806.06438*.
[50] J. Liu, Y. Sun, X. Xu, and U. S. Kamilov, "Image restoration using total variation regularized deep image prior," in *Proc. IEEE Int. Conf. Acoust., Speech Signal Process.*, 2019, pp. 7715–7719.
[51] D. Liu, V. Kolehmainen, S. Siltanen, A.-M. Laukkanen, and A. Seppänen, "Nonlinear difference imaging approach to three-dimensional electrical impedance tomography in the presence of geometric modeling errors," *IEEE Trans. Biomed. Eng.*, vol. 63, no. 9, pp. 1956–1965, Sep. 2016.
[52] B. Gong, B. Schullcke, S. Krueger-Ziolek, F. Zhang, U. Mueller-Lisse, and K. Moeller, "Higher order total variation regularization for EIT reconstruction," *Med. Biol. Eng. Comput.*, vol. 56, no. 8, pp. 1367–1378, 2018.
[53] M. Jaderberg et al., "Population based training of neural networks," 2017, *arXiv:1711.09846*.
[54] K. He, X. Zhang, S. Ren, and J. Sun, "Identity mappings in deep residual networks," in *Proc. Eur. Conf. Comput. Vis.*, Springer, 2016, pp. 630–645.
[55] K. C. Zhou and R. Horstmeyer, "Diffraction tomography with a deep image prior," *Opt. Exp.*, vol. 28, no. 9, pp. 12872–12896, 2020.
[56] H. Wang, T. Li, Z. Zhuang, T. Chen, H. Liang, and J. Sun, "Early stopping for deep image prior," 2021, *arXiv:2112.06074*.
[57] Z. Cheng, M. Gadelha, S. Maji, and D. Sheldon, "A Bayesian perspective on the deep image prior," in *Proc. IEEE/CVF Conf. Comput. Vis. Pattern Recognit.*, 2019, pp. 5443–5451.
[58] R. M. Neal, *Bayesian Learning for Neural Networks*. Berlin, Germany: Springer Science & Business Media, 2012, vol. 118.
[59] S. Liu, J. Jia, Y. D. Zhang, and Y. Yang, "Image reconstruction in electrical impedance tomography based on structure-aware sparse Bayesian learning," *IEEE Trans. Med. Imag.*, vol. 37, no. 9, pp. 2090–2102, Sep. 2018.
[60] S. Liu, Y. Huang, H. Wu, C. Tan, and J. Jia, "Efficient multitask structure-aware sparse Bayesian learning for frequency-difference electrical impedance tomography," *IEEE Trans. Ind. Informat.*, vol. 17, no. 1, pp. 463–472, Jan. 2021.
[61] G. Ma, H. Chen, P. Wang, and X. Wang, "Multi-frame constrained block sparse Bayesian learning for flexible tactile sensing using electrical impedance tomography," *IEEE Trans. Comput. Imag.*, vol. 8, pp. 438–448, 2022.
[62] K. Zhang, Y. Li, W. Zuo, L. Zhang, L. Van Gool, and R. Timofte, "Plug-and-play image restoration with deep denoiser prior," *IEEE Trans. Pattern Anal. Mach. Intell.*, vol. 44, no. 10, pp. 6360–6376, Oct. 2022.

Dong Liu (Senior Member, IEEE) received the PhD degree in applied physics from the University of Eastern Finland, Kuopio, Finland, in 2015. From 2016 to 2022, he had been with the School of Physical Sciences, University of Science and Technology of China. From 2023, he is a research professor with the Division of Life Sciences and Medicine, University of Science and Technology of China. His research interests broadly include applied inverse problems and medical imaging. He currently focuses primarily on the development of model-driven and learning based algorithms for inverse problems that arise in a variety of biomedical and engineering applications, including, but not limited to, electrical impedance tomography.

Junwu Wang received the BS degree from the School of Mathematical Sciences, University of Science and Technology of China (USTC), in 2019. He is currently working toward the PhD degree with the School of Mathematical Sciences, University of Science and Technology of China. His research interests include electrical impedance tomography and positron emission tomography.

Qianxue Shan received the BS degree from the Soochow University, in 2021. She is currently working toward the master's degree with the CAS Key Laboratory of Microscale Magnetic Resonance supervised by prof. Dong Liu. She currently studies in University of Science and Technology of China. Her research interests include positron emission tomography and deep neural network.

Danny Smyl received the BS and MS degrees in civil engineering from the University of Kansas, Lawrence, KS, USA, and the PhD degree in civil engineering from North Carolina State University, Raleigh, NC, USA. He has served as an officer with the U.S. Marine Corps. He is now a professor of structural engineering with the University of South Alabama. Some of his research interests include deep learning, structural health monitoring, infrastructure materials, and medical imaging.

Jiansong Deng received the undergraduate, the master's and PhD degrees from the University of Science and Technology of China (USTC), Hefei, China. Since 2005, he has been a professor with the Department of Mathematics/School of Mathematical Sciences, USTC. His research interests include geometric modeling and applied approximation theory. He currently focuses on spline spaces over T-meshes and their application in geometric modeling and numerical solutions of partial differential equations.

Jiangfeng Du received the undergraduate, master's, and PhD degrees from the University of Science and Technology of China (USTC), Hefei, China. Since 2004, he has been a professor with the School of Physical Sciences, USTC, where he served as the vice-president. From December 2022, he has been nominated as the president of Zhejiang University. He is currently a member of the Chinese Academy of Sciences, Beijing, China. He and his team developed a series of advanced spin quantum control methods to precisely manipulate spin quantum states and several kinds of advanced magnetic resonance spectrometers. His research interest is interdisciplinary. He also focuses on quantum computation, quantum information, and quantum sensing, and the development of new technologies for medical applications.